# Effect of Zr Impregnation on Clay-Based Materials for H₂O₂-Assisted Photocatalytic Wet Oxidation of Winery Wastewater

**Vanessa Guimarães \*** [ID]**, Ana R. Teixeira, Marco S. Lucas** [ID] **and José A. Peres** [ID]

Vila Real Chemistry Center (CQVR), University of Trás-os-Montes and Alto Douro (UTAD), Quinta de Prados, 5000-801 Vila Real, Portugal; ritamourateixeira@gmail.com (A.R.T.); mlucas@utad.pt (M.S.L.); jperes@utad.pt (J.A.P.)

**\*** Correspondence: guimavs@gmail.com

**Abstract:** UV-activated Zr-doped composites were successfully produced through the impregnation of Zr on the crystal lattice of different clay materials by a one-step route. Fixing the amount of Zr available for dopage (4%), the influence of different supports, submitted to different chemical treatments, on the photocatalytic activity of the resulting Zr-doped pillared clay materials (PILC) was assessed. Both chemical characterization and structural characterization suggest that the immobilization of Zr on montmorillonite and PILC structures occurred through isomorphic substitution between Si and Zr in the tetrahedral sheet of the clay material. This structural change was demonstrated by significant modifications on Si-OH stretching vibrations (1016 cm$^{-1}$, 1100 cm$^{-1}$ and 1150 cm$^{-1}$), and resulted in improved textural properties, with an increase in surface area from 8 m$^2$/g (natural montmorillonite) to 107 m$^2$/g after the pillaring process, and to 118 m$^2$/g after the pillaring and Zr-doping processes ((Zr)Al-Cu-PILC). These materials were tested in the UV-photodegradation of agro-industrial wastewater (AIW), characterized by high concentrations of recalcitrant contaminants. After Zr-dopage on AlCu-PILC heterogeneous catalyst, the total organic carbon (*TOC*) removals of 8.9% and 10.4% were obtained through adsorption and 77% and 86% by photocatalytic oxidation, at pH 4 and 7, respectively. These results suggest a synergetic effect deriving from the combination of Zr and Cu on the photocatalytic degradation process.

**Keywords:** Zr-doped materials; pillared clays; advanced oxidation processes; photocatalysis; agro-industrial wastewater

## 1. Introduction

Agro-industrial activities are one of the main sources of wastewater pollution and its impact on the environment has received special attention in recent years [1,2]. Winery wastewater (WW) is characterized by high load of recalcitrant organic compounds [1,3], and its unregulated discharge represents a great threat to aquatic ecosystems and human health [4]. In this regard, the development of effective and low cost methods for the treatment of WW is now imperative.

Currently, different techniques have been developed to treat this type of effluent, including adsorption [5], coagulation [6] and biological processes [7]. However, some of the drawbacks include the limited adsorption capacity and the formation of a potential second pollution source, since these processes only transfer contaminants from one phase to another instead of destroying them [8]. Biological degradation is the most common process applied, however, the microbial activity can be inhibited by the recalcitrant character and toxicity of the organic contaminants [9]. To overcome these problems, advanced oxidation processes (AOPs) have been proposed as effective, fast and non-expensive

technologies for the degradation of recalcitrant contaminants [10–12]. Different homogeneous AOPs have already been applied in the treatment of agro-industrial wastewaters, particularly ozonation [13], Fenton [14] and photo-Fenton (solar and UV-A LEDs) processes [15]. Nonetheless, despite the interesting results obtained, Fenton processes have important limitations, namely the acidic conditions needed to improve the degradation efficiency, the additional procedure to remove the homogeneous catalyst from treated effluent, and the neutralization of the treated effluent to meet the legal discharge limits (pH 6.0–9.0) [16]. In order to overcome these drawbacks, heterogeneous AOPs have been the main focus of research interest in the last years, due to the substantial reduction in the effective costs associated with the sludge treatment, as well as the easy catalyst recovery and potential reuse [17,18].

The Catalytic Wet Peroxide Oxidation (CWPO) process is one of the most efficient, economical and environmental-friendly advanced oxidation processes for the treatment of non-biodegradable pollutants under milder conditions, and was successfully applied in the treatment of several organic contaminants, using different types of supports [19–22]. Considering the recalcitrant character of some type of effluents and the fairly poor results that have been obtained so far with the conventional Fenton process, the combination of UV light irradiation in the oxidation processes was proposed with a significant improvement in degradation efficiency [22–26].

The application of CWPO process in the treatment of WW is quite limited. Among our previous research studies, where different clay-based supported catalysts were applied for the first time in the heterogeneous UV/$H_2O_2$-assisted treatment of a real winery wastewater [27,28], only few heterogeneous catalysts including Fe-graphite [29] and natural clay [30] were applied to improve the efficiency of CWPO in the treatment of a winery wastewater. The results obtained by other studies are very interesting, with significant *TOC* removals, 80% and 55%, respectively. However, the authors did not explore the influence of crucial operational conditions, namely the variation of pH conditions, which may affect the efficiency of the photo-catalytic process.

According to our previous studies, the application of AlCu pillared clay (PILC) as heterogeneous catalyst revealed great stability along the treatment process and a high performance at neutral pH conditions, reaching a *TOC* removal of 83% ([$H_2O_2$]$_0$ = 98 mM; catalyst dosage = 3.00 g/L). This is particularly important, once it allows the catalyst reuse and eliminates the cost of effluent neutralization before its discharge. Thus, in this work, a novel Zr-doped AlCu-pillared clay ((Zr)AlCu-PILC) was prepared, attending to the $ZrO_2$ excellent electrical, mechanical, chemical and photocatalytic properties. Accordingly, AlCu-PILC was chosen for this purpose owing to their low cost, environmental stability, high surface area and adsorption capacity, as well as great photo-catalytic activity, which combined with Zr may be significantly enhanced [20,21]. Zr-nanocomposites have been prepared by quite a few methods, including the sol–gel process [31,32], combustion [33], the hydrothermal method [34], microwave irradiation [35], etc. However, it continues to be a challenge to find a simple, efficient and low cost methodology to prepare these nanocomposites.

This work intends to develop a one-step route to incorporate Zr onto clay lattice, promoting great stability and improved photocatalytic activity. The resulting photocatalyst will be tested in the photodegradation of a real WW under UV-C irradiation, and the influence of Zr immobilization on the properties and photoactivity of the heterogeneous catalysts will be discussed.

Different models have been employed to describe the kinetics of catalytic processes involving a heterogeneous liquid–solid system [36–38]. Reaction control models, such as pseudo-first-order and pseudo-second-order models, were considered unsuitable to describe the kinetics of heterogeneous photocatalytic processes, because the two separated linear regression analyses obtained did not take into account relevant factors, namely, the transient period between each linear region, the non-linear behavior during the induction period, and the objective determination of each region, which is subjective when applying two separated linear regressions. The Fermi's model provides a single fit to experimental results showing a transition between the induction period (slow degradation) and the subsequent rapid degradation step of an organic compound (inverted S-shaped transient curve) [39–41]. Considering that the degradation process does not have to follow any particular kinetics or reaction

order, it is worth noting that Fermis based model was specifically developed to describe the kinetics of complex systems, involving mixtures of unknown pollutants and several reaction intermediates formed during the photocatalytic process. Therefore, it includes lumped analytical parameters, such as *TOC*, that can be derived in groups of compounds with different reactivity [42].

In a previous work [42], a lumped kinetic model based on Fermi's equation was developed to describe the *TOC* histories for the degradation of a dye by catalytic wet peroxide oxidation, as shown in Equation (1)

$$\frac{TOC}{TOC_0} = \frac{1 - x_{TOC}}{1 + \exp\left[k_{TOC}(t - t_{TOC}^*)\right]} + x_{TOC} \tag{1}$$

where $k_{TOC}$ corresponds to the apparent reaction rate constant; $t_{TOC}^*$ represents the transition time related to the *TOC* content curve's inflection point, and $x_{TOC}$ corresponds to the fraction of non-oxidazable compounds that are formed during the reaction.

The Lumped kinetic model based on Fermi's equation has successfully described the kinetics of our previous experiments using pillared clays in the $H_2O_2$-assisted photocatalytic wet oxidation of WW and, therefore, it is intended to apply this method in order to describe the kinetics of the WW degradation process using the new proposed materials as heterogeneous catalysts.

## 2. Materials and Methods

### 2.1. Reagents and Winery Wastewater Sampling

$ZrOCl_2.8H_2O$ (99%) was supplied by Alfa-Aesar, $CuCl_2.2H_2O$ (99%) by Panreac, $H_2O_2$ (30% *w/v*) by Sigma-Aldrich. NaOH and $H_2SO_4$ (95%) were both obtained from Analar NORMAPUR. Deionized water was used to prepare the respective solutions. The agro-industrial wastewater (AIW) was collected from a Portuguese winery cellar located in the Douro region (Northeast of Portugal). The main chemical parameters measured are shown in Table 1. Prior to the oxidation process, the wastewater was submitted to a primary treatment, where the suspended solids were removed from the effluent.

**Table 1.** Agro-industrial wastewater characterization.

| Parameter | Value |
|:---:|:---:|
| pH | 3.8 ± 0.1 |
| Chemical Oxygen Demand (mg $O_2$/L) | 1420 ± 45 |
| Biochemical Oxygen Demand (mg $O_2$/L) | 610 ± 15 |
| Total Organic Carbon (mg C/L) | 500 ± 12 |
| Total Polyphenols (mg gallic acid/L) | 105 ± 3 |
| Phosphates (mg $P_2O_5$/L) | 2.7 ± 0.2 |
| Sulphates (mg $SO_4^{2-}$/L) | 17.8 ± 1.0 |
| Total Iron (mg Fe/L) | 0.45 ± 0.02 |
| Aluminium (µg Al/L) | 17.5 ± 0.9 |
| Cadmium (µg Cd/L) | 2.1 ± 0.1 |
| Copper (µg Cu/L) | 400 ± 18 |
| Chromium (µg Cr/L) | 0.05 ± 0.003 |
| Manganese (µg Mn/L) | 29 ± 1.4 |
| Zinc (µg Zn/L) | 4200 ± 200 |

### 2.2. Clay Mineral

Natural montmorillonite (MT) was purchased from Fluka, Alfa-Aesar. The chemical composition and main surface properties of natural clay mineral are listed in Tables 2 and 3, respectively. The chemical data was determined by energy dispersive X-ray spectroscopy (EDS/EDAX, FEI QUANTA–400). The total iron expressed as $Fe_2O_3$ content in raw-montmorillonite was found to be 4.28%. The cation exchange capacity (CEC) of the mineral fractions was measured following the ammonium acetate method proposed by Chapman [43].

**Table 2.** Main chemical compositions of raw montmorillonite and its derived catalysts, obtained by EDS/EDAX (wt.%).

| Sample | SiO$_2$ (%) | Al$_2$O$_3$ (%) | Fe$_2$O$_3$ (%) | MgO (%) | Na$_2$O (%) | CaO (%) | K$_2$O (%) | CuO (%) | ZrO$_2$ (%) | Al/Si | Zr/Si | CEC (meq/g) |
|---|---|---|---|---|---|---|---|---|---|---|---|---|
| MT | 68.80 | 21.97 | 1.58 | 3.13 | 2.54 | 0.95 | 0.31 | - | - | 0.32 | - | 0.61 |
| Zr-MT | 63.35 | 20.09 | 1.50 | 2.90 | 2.90 | 0.85 | 0.31 | - | 5.54 | 0.32 | 11.44 | 0.22 |
| AlCu-PILC | 64.15 | 26.36 | 1.36 | 2.53 | 0.97 | 0.26 | 0.37 | 1.32 | - | 0.41 | - | 0.23 |
| (Zr)Al-PILC | 60.66 | 25.62 | 1.69 | 2.15 | 1.17 | 0.56 | 0.6 | - | 5.14 | 0.42 | 11.80 | 0.21 |
| (Zr)AlCu-PILC | 60.46 | 25.64 | 1.03 | 1.97 | 1.02 | 0.24 | 0.23 | 1.30 | 5.41 | 0.42 | 11.18 | 0.22 |

**Table 3.** Specific surface areas and pore characteristics of MT and their respective catalysts.

| Sample | S$_{BET}$ (m$^2$/g) | V$_{total\ pore}$ (cm$^3$/g) |
|---|---|---|
| MT | 8.5 | 0.047 |
| Zr-MT | 65 | 0.109 |
| Al-Cu-PILC | 107 | 0.202 |
| (Zr)Al-PILC | 81 | 0.146 |
| (Zr)Al-Cu-PILC | 118 | 0.217 |

### 2.3. Analytical Techniques

Several physical-chemical parameters were measured in order to characterize the agro-industrial wastewater, namely the chemical oxygen demand (COD), the biological oxygen demand (BOD$_5$), the total organic carbon (*TOC*) and the total polyphenols (mg gallic acid/L) presented in Table 1. The COD and BOD$_5$ were determined according to Standard Methods (5220D; 5210D; respectively) [44]. COD analysis was carried out in a COD reactor from HACH Co. and a HACH DR 2400 spectrophotometer was used for colorimetric measurement. Biochemical oxygen demand (BOD$_5$) was determined using a respirometric OxiTop system. pH evolution was followed by means of a pH-meter (HANNA Instruments, Rhode Island, USA). The *TOC* content (mg C/L) was determined using a Shimadzu *TOC*-L CSH analyzer (Tokyo, Japan). Total polyphenols were evaluated following the Folin–Ciocalteu method [45].

### 2.4. Catalysts Preparation

The preparation of the pillared clays was carried out following a conventional procedure described in detail by Molina, et al. [46]. AlCu-PILC was prepared through the intercalation between montmorillonite fractions and poly(hydroxy)aluminium (Al$_3$(OH)$_4^{5+}$) and copper Cu$_3$(OH)$_4^{2+}$ species. The pillaring solution was prepared by slow addition of a 0.2 M NaOH solution to a mixture of 0.1 M AlCl$_3$ and 0.1 M CuCl$_2$ (Cu/(Al+Cu) = 0.1), under constant stirring until the molar ratio OH/Al = 2.5 was reached. The resulting solution was adjusted to pH 6 and was further aged for 8 h at 298 K. The intercalation process was initiated by the addition of a suspension of 0.1 wt.% montmorillonite in deionized water to the pillaring solution, applying the stoichiometry of 10 mmol Al/g clay. The cationic exchange process was carried out at room temperature for 12 h under constant stirring. The resulting suspension was washed by centrifugation with deionized water in order to reach ionic conductivity values lower than 10 μS. After air-drying, the resulted material was calcined for 2 h at 400 °C.

The Al-Cu oligomeric solution was adjusted to pH 6 in order to achieve the higher proportion of oligomeric species: 100% of both Al$_3$(OH)$_4^{5+}$ and species. The aqueous speciation was calculated by Visual MINTEQ, version 3.0. After the pillaring process, Cu$^{2+}$ oligomeric species were converted to the respective metal oxide clusters by dehydration and dehydroxylation along the calcination process. The Al-PILC was prepared following the same procedure adopted to AlCu-PILC, but only using poly(hydroxy)aluminium (Al$_3$(OH)$_4^{5+}$) species.

The Zr-doped catalysts (Zr-MT, (Zr)Al-PILC and (Zr)AlCu-PILC)) were prepared by the incipient wetness impregnation method. The precursor solution was prepared with ZrOCl$_2$.8H$_2$O in order to

obtain a zirconium load of 4 wt.%. After impregnation process, the doped catalysts were dried at 100 °C overnight and calcinated for 3 h at 400 °C. The results obtained from the chemical characterization (Table 2) confirm that 4 wt.% of zirconium were successfully immobilized on different heterogeneous catalysts.

## 2.5. Catalysts Characterization

The FTIR spectra were obtained by mixing 1 mg natural montmorillonite with 200 mg KBr. The powder mixtures were then inserted into molds and pressed at 10 ton/cm$^2$ to obtain the transparent pellets. The samples were analyzed with a Bruker Tensor 27 spectrometer and the infrared spectra in transmission mode were recorded in the 4000–400 cm$^{-1}$ frequency region. The microstructural characterization was carried out by scanning electron microscopy (SEM/ESEM FEI QUANTA 400) and the chemical composition of the different catalysts was estimated (Table 2) using energy dispersive X-ray spectroscopy (EDS/EDAX).

The textural parameters of samples were obtained from N$_2$ adsorption–desorption isotherms at 77 K using a Micromeritics ASAP 2020 apparatus (Norcross, Georgia, USA). The samples were degassed at 150 °C up to 10$^{-4}$ Torr before analysis. The specific surface area ($S_{BET}$) was determined by applying the Gurevitsch's rule at a relative pressure p/p$_0$ = 0.30 and according to the Brunauer, Emmet, Teller (BET) method from the linear part of the nitrogen adsorption isotherms. Different pore volumes were determined by the Barrett, Joyner, Halenda model (BJH model).

## 2.6. Adsorption Tests

Different adsorption tests were carried out in order to predict the amount of organic carbon removed through adsorption. The adsorption batch experiments were carried out at different pH conditions (pH 4.0 and pH 7.0) by adding 3.00 g/L of each heterogeneous catalyst into 500 mL of WW (500 mg C/L). The temperature was kept constant throughout the experiments. After the adsorption runs, the samples were centrifuged and the *TOC* content of the supernatant solution was measured. The percentage of organic carbon removed through adsorption was calculated according to Equation (2) [47,48]:

$$TOC_{rem.}(\%) = \frac{TOC_0 - TOC_t}{TOC_0} \times 100 \tag{2}$$

where $TOC_0$ is the initial *TOC* content (mg C/L) and $TOC_t$ is *TOC* value at instant $t$ (mg C/L).

## 2.7. Photocatalytic Experiments and Kinetic Modelling

The photocatalytic experiments were performed in a batch cylindrical photoreactor (600 cm$^3$) equipped with a UV-C low pressure mercury vapour lamp (TNN 15/32)—working power = 15 W (795.8 W/m$^2$) and $\lambda_{max}$ = 254 nm (Heraeus, Germany). The UV absorption spectrum of the AIW reveals a maximum at ca. 275 nm (with and without the catalysts) and a high absorption at the wavelength where the UV-C lamp emits. In a typical run, 3.0 g/L of catalyst was mixed with 500 mL of the AIW (*TOC* = 500 mg C/L) for 15 min. After this, a specific amount of H$_2$O$_2$ (98 mM) was added to the suspension and the UV light was turned on at the same time. The initial pH varied from 4.0 to 7.0, and was adjusted by adding 1 M of H$_2$SO$_4$ or 1 M of NaOH. After the reaction has started, 20 mL of solution was withdrawn for *TOC* measurements at different reaction times, completing a total period of 240 min. The samples were centrifuged and the Zr and Cu concentrations were analyzed by atomic absorption spectroscopy (AAS) using a Thermo Scientific iCE 3000 SERIES. All experiments were performed in triplicate and the observed standard deviation was always less than 5% of the reported values.

A kinetic modelling based on a lumped kinetic model traduced by Fermi's equation was carried out in order to describe the WW degradation process. The experiments were conducted at different pH conditions (pH 4 and pH 7), where temperature, effluent volume, contaminant concentration, H$_2$O$_2$ concentration and catalyst dosage were kept constant. A nonlinear least squares regression,

based on the Levenberg–Marquardt (LM) algorithm, was applied using the OriginPro 8.5 "Sigmoidal Fit Tool". As a result, a unique semi-empirical function is applied to simultaneously describe the initial low *TOC* conversion (induction period) and subsequent rapid degradation step. Therefore, both the initial transition period and pseudo-first order kinetic period can be expressed with the proposed model [49].

## 3. Results and Discussion

### 3.1. Catalysts Characterization

The X-ray diffractograms corresponding to natural montmorillonite (MT) and to Zr-doped and undoped PILCs, are shown in Figure 1. The hkl reflections associated with MT diffraction pattern are characteristic of a montmorillonite clay mineral with mixed interlayer composition including different proportions of $Na^+$ and $Ca^{2+}$ ions (13.08 Å). This assumption is in agreement with the chemical characterization data, which shows proportions of 0.95% and 2.54% of CaO and $Na_2O$ (Table 2), respectively. The MT samples modified with previously synthesized oligomeric species ($Cu_3(OH)_4{}^{2+}$ and/or $Al_3(OH)_4{}^{5+}$ show a shift of the basal reflection d001 from 13.08 Å (MT) to 18.02 Å and to 17.01 Å for (Zr)AlCu-PILC and (Zr)Al-PILC, respectively, confirming the insertion of the oligomeric species in the interlayer region of montmorillonite and the successful pillaring process. The higher expansion observed when both Cu- and Al-oligomeric species were intercalated on montmorillonite results from the higher pillars formed, indicating that the number, charge, size and shape of the oligomeric species affect the pillar size. These results were also suggested by the textural properties obtained for these materials (Table 3), since the (Zr)AlCu-PILC has higher surface area (ABET=x) and higher number of total pore volume than (Zr)Al-PILC, suggesting an increase in contact area available for absorption due to the higher pillars formed.
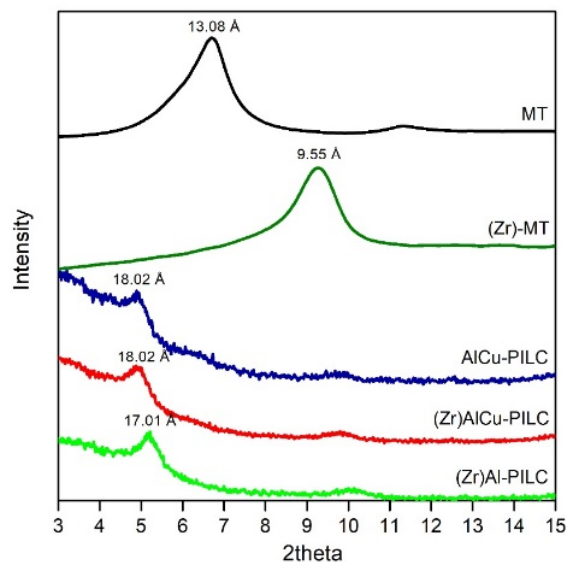


**Figure 1.** X-ray diffraction results obtained before (MT) and after the pillaring process (AlCu-PILC) and Zr-dopage ((Zr)-Al-PILC, (Zr)AlCu-PILC).

Comparing both (Zr)AlCu-PILC and AlCu-PILC diffraction patterns, it is possible to observe an identical behaviour, confirming that Zr was probably incorporated into the AlCu-PILC lattice without structural modification. The chemical composition of both samples before and after the Zr-doping process is also in agreement with this previous conclusion, given that the increase in Zr amount in doped-clay minerals is accompanied by a decrease in Si proportion, suggesting the isomorphic substitution between Si and Zr in the tetrahedral sheet of the pillared clay. This mechanism is triggered by the similar ionic radii of both cations, where the new one may have identical or lower ionic charge

than the replaced one. In this case, both Si and Zr have similar ionic radii and the same ionic charge (+4) and, therefore, no structural charge was developed and no significant structural changes have occurred. This is particularly important, because once the AlCu-PILC has not been structurally affected by the doping process, the adsorption capacity, which is crucial for its catalytic activity, was also not negatively affected. Moreover, enhanced catalyst stability is expected; once Zr is directly incorporated on the crystal lattice of montmorillonite, the risk of metal leaching is significantly lower.

Comparing both (Zr)-MT and MT spectra, no additional conclusions are achieved, since, after the Zr impregnation process, sample (Zr)-MT was submitted to the calcination process, which resulted in the total interlayer collapse to 9.55 Å by dehydration. Therefore, independently of the position of Zr (tetrahedral sheet or interlayer region) on the MT structure, the structural collapse will occur and avoid additional conclusion by means of X-ray diffraction (XRD).

Figure 2 depicts the FTIR spectra obtained before (MT) and after the pillaring process (AlCu-PILC), as well as before (AlCu-PILC) and after the Zr-doping process ((Zr)AlCu-PILC). The results show some structural alterations on montmorillonite after the uptake of metal poly(hydroxy)-complexes and consequent formation of pillars on its internal surface. This is traduced by the decrease in intensity and shift of peaks in the range between 800 and 950 cm$^{-1}$, after the pillaring process, which are assigned to Al-OH, Fe-OH and Mg-OH vibration modes, at 916 cm$^{-1}$, 877 cm$^{-1}$ and 849 cm$^{-1}$, respectively. These structural changes were only observed for PILC samples, which, according to Zhou et al. [50], can be attributed to the interactions between Al or Al/Cu mixed poly(hydroxy) species and the alumina octahedral layers.

Significant modifications on Si-OH stretching vibrations were observed after the Zr-doping process, due to the shift of the main band from 1016 cm$^{-1}$ to 1040 cm$^{-1}$, and the reduction in intensity of the additional stretching vibrations assigned to the Si-O group, at 1150 cm$^{-1}$ and 1100 cm$^{-1}$, confirming the incorporation of Zr ions directly in the crystal lattice by isomorphic substitution of Si ions in the tetrahedral sheet of montmorillonite. On the other hand, no additional changes in the vibrations associated with the octahedral sheets of montmorillonite (800–950 cm$^{-1}$) were observed after this process.
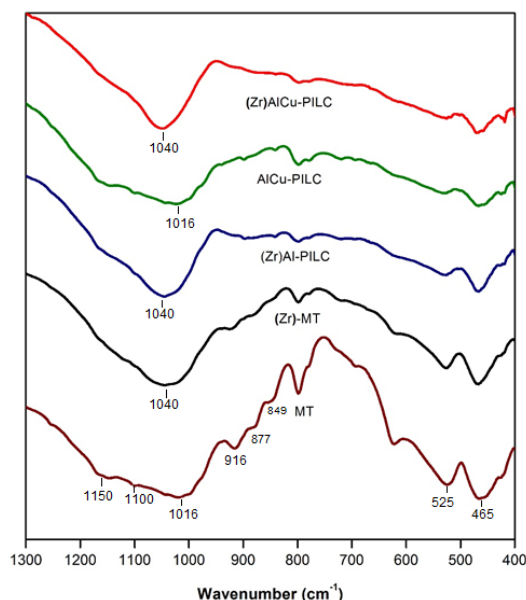


**Figure 2.** FTIR results obtained before (MT) and after pillaring process (AlCu-PILC) and Zr-dopage ((Zr)-Al-PILC, (Zr)AlCu-PILC), Zr-MT.

The specific surface area and total pore volume of the original montmorillonite and doped and undoped materials are shown in Table 3. These results suggest significant alterations on montmorillonite after the pillaring and Zr-doping processes, resulting in significant and progressive increases in surface

area and total pore volume. Accordingly, the surface area increased from 8 $m^2/g$ (MT) to 107 $m^2/g$ after the pillaring process, and to 118 $m^2/g$ after the pillaring and Zr-doping processes, whereas the total pore volume increased from 0.05 $cm^3/g$ (MT) to 0.20 $cm^3/g$ and to 0.22 $cm^3/g$ for AlCu-PILC and (Zr)AlCu-PILC, respectively. The respective isotherms can be classified as type II, where unrestricted monolayer–multilayer adsorption occurs, and the behaviour of the hysteresis loops can be associated with type H3, which usually corresponds to aggregates of plate-like particles forming slit-like pores, which is in agreement with these material structures.

*3.2. Adsorption vs. Reaction*

Adsorption experiments were carried out using the pillared and Zr-doped catalysts to evaluate the effect of their surface chemistry on the contaminant adsorption and *TOC* removal. According to previous studies, adsorption plays an important role as the main mechanism involved in the initial induction period, which corresponds to the period necessary for catalyst surface activation [51]. In the present study, part of the mechanism associated with the induction period is probably associated with the adsorption of $H_2O_2$ and organic compounds onto the catalyst surface, producing surface complexes which promote the activation of the oxidation process through the generation of HO• radicals. Our previous research assessed, for the first time, the application of natural pillared clays (PILCs: Al-Cu-ST and Al-Fe-ST) as heterogeneous photocatalysts for the $H_2O_2$-assisted treatment of a real AIW [27]. The results indicated that the transition point between the induction period and surface activation and the production of HO• species was directly influenced by the amount of $H_2O_2$ initially dosed to the process. Accordingly, a decrease in the transition period (t *) *TOC* from 136 to 96 min was observed, using Al-Cu-ST as the heterogeneous catalyst (3.0 g/L), when $H_2O_2$ concentration increased from 29 to 98 mM, reducing the period necessary for the surface activation and, therefore, the period required to initiate the degradation process. Considering our previous conclusions, the influence of different catalysts, as well as the effect of Zr-dopage on these supports, were evaluated, taking into account the optimal experimental conditions obtained before, namely $[H_2O_2]_0$ = 98 mM and catalyst dosage = 3.0 g/L.

The evolution of *TOC* removal through adsorption at different pH conditions and using the different catalysts is shown in Figure 3. As expected, both pH conditions imposed and catalyst textural properties affected the catalyst adsorption capacity. The lowest contaminant adsorption was obtained for Zr-MT and (Zr)Al-PILC, at pH 4 and pH 7, respectively, which correspond to the catalysts with lower surface area (65 $m^2/g$ and 81 $m^2/g$, respectively). On the contrary, the higher adsorption capacity was obtained for (Zr)AlCu-PILC, at both pH conditions, corresponding to the sample with the highest surface area (118 $m^2/g$) and total pore volume (0.22 $cm^3/g$) obtained. This behaviour has particularly impact on the *TOC* removal efficiency along the oxidation process (Figure 4), as it is observed that the catalyst with enhanced adsorption capacity at both pH conditions has greater activity in the degradation process. Accordingly, the *TOC* removals obtained using (Zr)AlCu-PILC/UV after 4 h, corresponds to 77% and 86%, at pH 4 and 7, respectively. The incorporation of Zr on montmorillonite lattice (Zr-MT) has contributed to the significant improvement of *TOC* removals, when compared with raw-montmorillonite, with an increase from 46% to 60% and from 37% to 61% at pH 4 and 7, respectively. The development of AlCu pillared structures had additional advantages considering the improvement of montmorillonite textural properties, resulting in additional stability and catalyst activity. This is traduced by the increase in *TOC* removals to 69% and 73% at pH 4 and 7, respectively, with a maximum of 33% removal in the non-catalytic UV-C/$H_2O_2$ experiments performed at both pH conditions. As previously observed, the Zr-dopage on AlCu-PILC has also improved its catalytic activity, promoting an increase in *TOC* removals to 77% and 86%, at pH 4 and pH 7, respectively, suggesting a synergetic effect of both Zr and Cu on the photocatalytic degradation process. In this case, Zr acts as a semiconductor that is excited by photons with an energy greater than its band gap (5.8–7.1 eV), generating electron–hole pairs, which migrates to the photocatalyst surface yielding radical species that can react with organic molecules upon redox reactions. The electron transfer

process is enhanced by the successive redox of $Cu^{2+}$, a transition metal which is continuously releasing e- species, induced by the presence of a permanent irradiation source (UV-C).

During these processes, a decrease in catalyst stability, caused by the increase in Cu leaching levels from 0.0 to 1.4 mg/L, was also observed from the acidic to the neutral conditions. However, all the Cu leaching concentrations are lower than or very close to the legal discharge limit imposed by EU legislation (1.0 mg Cu/L), and only 5.0% of the Cu immobilized was released at neutral conditions, confirming that Cu immobilization on pillared clay support was successful.
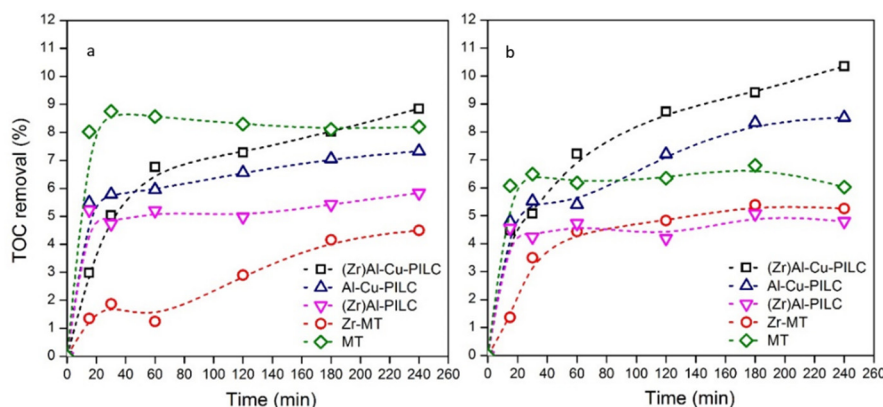


**Figure 3.** Evolution of *TOC* removal by adsorption: (**a**) pH 4.0 and (**b**) pH 7.0 (catalyst dosage = 3.0 g/L, $[TOC]_0$ = 500 mg C/L).

Comparing both Zr-MT and (Zr)Al-PILC performances at both pH conditions, it is possible to conclude that Zr-MT has shown increased catalytic activity, mainly from 180 min, with *TOC* removals of 60% at both pH conditions for Zr-MT, and 46% at both pH conditions for (Zr)Al-PILC. This behavior could be explained by the competition between Zr and an excess of Al for the Si tetrahedral sites on (Zr)Al-PILC, which may have hampered the Zr incorporation onto the montmorillonite crystal lattice. The lower catalytic activity observed using (Zr)Al-PILC is even more pronounced in acidic conditions, where the *TOC* conversion is very similar to MT along the treatment process. This could be explained by the increased adsorption capacity obtained by MT at pH 4.0 (Figure 3), associated with its higher CEC (Table 2), which despite the lower BET surface area of MT, when compared with (Zr)Al-PILC, has contributed to enhanced adsorption capacity and improved catalytic activity.
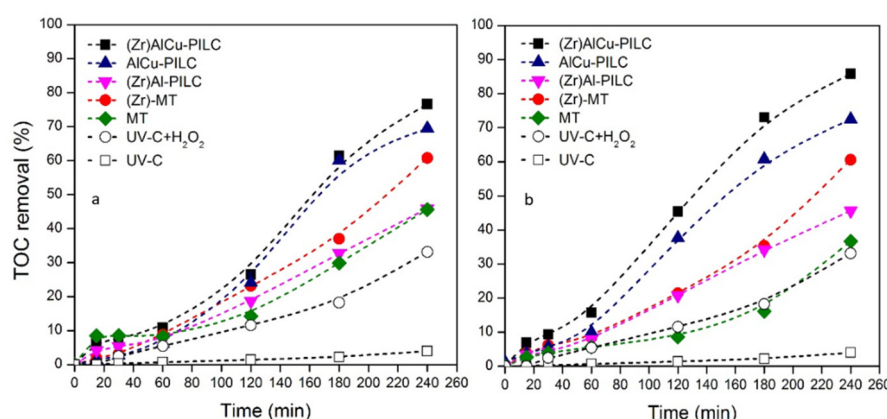


**Figure 4.** Evolution of *TOC* removal throughout $H_2O_2$-assisted photocatalytic process: (**a**) pH 4 and (**b**) pH 7 (catalyst dosage = 3.0 g/L, $[H_2O_2]_0$ = 98 mM, $[TOC]_0$ = 500 mg C/L).

### 3.3. Kinetic Study

In order to better understand the effect of the operational conditions on the induction period, the transition time between the induction period and the fast oxidation reaction (*t \* TOC*) was obtained

through the fitting of Fermi's equation based on lumped kinetic model to the experimental data. The results obtained for the different parameters are displayed in Table 4, and the fittings obtained for different catalysts are illustrated in Figure 5. The results reveal a good fitting of the kinetic model to the experimental data obtained for different catalysts, with $R^2$ values higher than 0.983. Considering the different parameters obtained from the modelling, it is assumed that the experimental conditions influenced the kinetic performance of our processes.
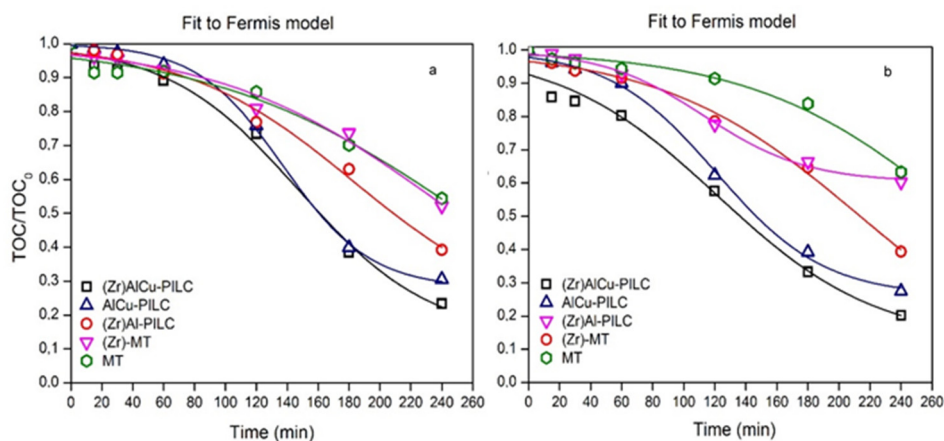


**Figure 5.** Normalized *TOC* content (*TOC/TOC*$_0$) as a function of time, using different pH conditions: (**a**) pH 4, (**b**) pH 7 (catalyst dosage = 3.0 g/L, $[H_2O_2]_0$ = 98 mM, $[TOC]_0$ = 500 mg C/L). Fit of Fermi's equation based on lumped kinetic model to the experimental data.

As observed in Figure 5, the transition point is significantly affected by the pH conditions, as well as the heterogeneous catalyst used. Accordingly, a significant decrease in $t * TOC$ was observed, from 279 to 121 min (pH 7) and from 253 to 137 min (pH 4), using raw-montmorillonite and AlCu-MT, respectively, suggesting a significant reduction in the surface activation period when the heterogeneous catalyst was applied, as well as a quicker production of $HO^\bullet$ species. This tendency was even more pronounced after Zr-dopage at neutral conditions, once the transition time has decreased from 121 to 119 min using (Zr)AlCu-PILC.

In both cases, the evolution of the $H_2O_2$ concentration along the photocatalytic experiments shows a decrease and subsequent increase in concentration in the first 60 min (Table 5), which suggests a possible adsorption and desorption of $H_2O_2$ on pillared montmorillonite. Therefore, the results suggest that the first 60 min of reaction were mainly associated with the formation of surface complexes between the $H_2O_2$ and catalyst surface, whereas the additional period, which completes the total induction period, may be associated with the time required for the surface activation, i.e., the time required for catalytic decomposition of the oxidant in the presence of the active phase (production of $HO^\bullet$).

Concerning the reaction rates of the different photocatalytic processes, higher reaction rates were observed using both (Zr)AlCu-PILC and AlCu-PILC catalysts when compared with the other catalysts applied (Table 4), confirming an improvement of catalytic performance during the oxidation processes. Comparing both catalysts, AlCu-PILC has the higher reaction rates at both pH conditions, $3.54 \times 10^{-2}$ min$^{-1}$ and $2.87 \times 10^{-2}$ min$^{-1}$, at pH 4 and 7, respectively. However, (Zr)AlCu-PILC ($k_{TOC} = 2.58 \times 10^{-2}$ min$^{-1}$) has contributed to lower fractions of non-oxidazable compounds formed during the reaction ($x_{TOC} = 0.11$, pH 7), when compared with AlCu-PILC ($x_{TOC} = 0.26$, pH 7), which is in agreement with the higher *TOC* removals obtained.

**Table 4.** Kinetic parameters obtained by fitting Fermi's model to the experimental data ($TOC/TOC_0$ as function of time) using different catalysts.

| Heterogeneous Catalyst | Variables | Kinetic Parameters | | | |
|---|---|---|---|---|---|
| | | $k_{TOC}$ (min$^{-1}$) | $t^*_{TOC}$ (min) | $x_{TOC}$ | $r^2$ |
| (Zr)AlCu-PILC | pH 4.0 | $2.35 \times 10^{-2}$ | 148 | 0.14 | 0.990 |
| | pH 7.0 | $2.58 \times 10^{-2}$ | 119 | 0.11 | 0.996 |
| AlCu-PILC | pH 4.0 | $3.54 \times 10^{-2}$ | 137 | 0.28 | 0.998 |
| | pH 7.0 | $2.87 \times 10^{-2}$ | 121 | 0.26 | 0.997 |
| (Zr)Al-PILC | pH 4.0 | $1.90 \times 10^{-2}$ | 158 | 0.45 | 0.992 |
| | pH 7.0 | $2.16 \times 10^{-2}$ | 140 | 0.50 | 0.993 |
| Zr-MT | pH 4.0 | $1.83 \times 10^{-2}$ | 183 | 0.19 | 0.983 |
| | pH 7.0 | $1.56 \times 10^{-2}$ | 214 | 0.0 | 0.990 |
| MT | pH 4.0 | $1.23 \times 10^{-2}$ | 253 | 0.0 | 0.960 |
| | pH 7.0 | $1.50 \times 10^{-2}$ | 279 | 0.0 | 0.980 |

**Table 5.** $H_2O_2$ removal in the photocatalytic experiments using different catalysts. General conditions: pH 4.0 and pH 7.0, catalyst dosage = 3.00 g/L, $[TOC]_0$ = 500 mg C/L, UV-C irradiation.

| Experiment Time (min) | | $H_2O_2$ Removal (%) | | |
|---|---|---|---|---|
| | | Blank ($H_2O_2$ Only) | (Zr)AlCu-PILC | AlCu-PILC |
| pH 4.0 | 0 | 0.00 | 0.00 | 0.00 |
| | 15 | 2.03 | 14.03 | 11.18 |
| | 30 | 9.03 | 10.88 | 9.73 |
| | 60 | 20.2 | 54.38 | 35.63 |
| | 120 | 38.3 | 47.39 | 41.89 |
| | 180 | 51.1 | 79.04 | 83.58 |
| | 240 | 62.0 | 96.86 | 93.13 |
| pH 7.0 | 0 | 0.00 | 0.0 | 0.00 |
| | 15 | 12.7 | 16.0 | 12.06 |
| | 30 | 8.61 | 12.9 | 10.05 |
| | 60 | 16.3 | 8.19 | 49.30 |
| | 120 | 28.5 | 45.6 | 53.29 |
| | 180 | 37.0 | 69.3 | 83.07 |
| | 240 | 46.0 | 88.4 | 94.69 |

*3.4. Catalyst Regeneration*

Considering the best performance of (Zr)AlCu-PILC, the catalyst reuse capacity was evaluated throughout three consecutive cycles of $H_2O_2$-assisted photocatalytic AIW treatment. The experiments were carried out at pH 7.0, using a catalyst dosage of 3.0 g/L and a $H_2O_2$ concentration of 98 mM. The results show that the *TOC* removal obtained using (Zr)AlCu-PILC corresponds to 86%, 66% and 63% after 240 min, for the first, second and third cycles, respectively. In general, a decrease in efficiency was observed from the first to the second cycle (with a loss of 20% in *TOC* removal). However, no additional loss of activity was observed from the second to the third cycle. All the leaching concentrations along the different cycles were very close to the legal limits imposed (1.0 mg Cu/L) and tended to decrease as the number of cycles increased, from 1.4 to 0.97 mg/L of Cu, from the first to the third cycle, revealing that the catalyst stability is not affected along the cycles.

**4. Conclusions**

Different catalysts submitted to different chemical treatments and/or the Zr-dopage process, were applied in the $H_2O_2$-assisted treatment of recalcitrant winery wastewater in order to evaluate

the influence of the surface chemical properties of the doped supports on their adsorption and catalytic properties.

FTIR results show that the incorporation of Zr in the crystal lattice of montmorillonite and PILC through isomorphic substitution between Si and Zr was traduced by significant modifications on Si-OH stretching vibrations, due to the shift of the main band from 1016 cm$^{-1}$ to 1040 cm$^{-1}$, and the decrease in intensity of the additional stretching vibrations assigned to the Si-O group, at, respectively, 1150 cm$^{-1}$ and 1100 cm$^{-1}$.

In general, the results show that Zr-dopage on AlCu-PILC has improved its adsorption and catalytic activity, promoting an increase in *TOC* removals to 77% and 86%, with 8.85% and 10.35% of *TOC* removed through adsorption, at pH 4 and pH 7, respectively. It suggests a synergetic effect caused by the combination of Zr and Cu on the photocatalytic degradation process, once the semiconductor electron transfer process is enhanced by the successive redox of Cu(II), induced by the presence of the UV-C irradiation source.

A significant decrease in $t * TOC$ was observed for AlCu-PILC and (Zr)AlCu-PILC, at both pH conditions, suggesting a significant reduction in the surface activation period when the heterogeneous catalyst was applied, as well as a quicker production of HO$^\bullet$ species. As a result, higher reaction rates were obtained using both (Zr)AlCu-PILC ($2.58 \times 10^{-2}$ min$^{-1}$) and AlCu-PILC ($k_{TOC} = 3.54 \times 10^{-2}$ min$^{-1}$) catalysts, confirming an improvement in catalytic performance along the oxidation processes. Comparing both catalysts, AlCu-PILC has the higher reaction rates at both pH conditions. However, (Zr)AlCu-PILC has contributed to lower fractions of non-oxidazable compounds formed during the reaction ($x_{TOC} = 0.11$, pH 7.0), making it a more efficient process.

## References

1. Amor, C.; Marchão, L.; Lucas, M.S.; Peres, J.A. Application of Advanced Oxidation Processes for the Treatment of Recalcitrant Agro-Industrial Wastewater: A Review. *Water* **2019**, *11*, 205. [CrossRef]

2. Ferreira, L.C.; Fernandes, J.R.; Rodríguez-Chueca, J.; Peres, J.A.; Lucas, M.S.; Tavares, P.B. Photocatalytic degradation of an agro-industrial wastewater model compound using a UV LEDs system: Kinetic study. *J. Environ. Manag.* **2020**, *269*, 110740. [CrossRef]

3. Noukeu, N.A.; Gouado, I.; Priso, R.J.; Ndongo, D.; Taffouo, V.D.; Dibong, S.D.; Ekodeck, G.E. Characterization of effluent from food processing industries and stillage treatment trial with *Eichhornia crassipes* (Mart.) and *Panicum maximum* (Jacq.). *Water Resour. Ind.* **2016**, *16*, 1–18. [CrossRef]

4. Sousa, R.M.O.F.; Amaral, C.; Fernandes, J.M.C.; Fraga, I.; Semitela, S.; Braga, F.; Coimbra, A.M.; Dias, A.A.; Bezerra, R.M.; Sampaio, A. Hazardous impact of vinasse from distilled winemaking by-products in terrestrial plants and aquatic organisms. *Ecotoxicol. Environ. Saf.* **2019**, *183*, 109493. [CrossRef]

5. Al Bsoul, A.; Hailat, M.; Abdelhay, A.; Tawalbeh, M.; Jum'h, I.; Bani-Melhem, K. Treatment of olive mill effluent by adsorption on titanium oxide nanoparticles. *Sci. Total Environ.* **2019**, *688*, 1327–1334. [CrossRef]

6. Chen, B.; Jiang, C.; Yu, D.; Wang, Y.; Xu, T. Design of an alternative approach for synergistic removal of multiple contaminants: Water splitting coagulation. *Chem. Eng. J.* **2020**, *380*, 122531. [CrossRef]

7.  Candia-Onfray, C.; Espinoza, N.; Sabino da Silva, E.B.; Toledo-Neira, C.; Espinoza, L.C.; Santander, R.; García, V.; Salazar, R. Treatment of winery wastewater by anodic oxidation using BDD electrode. *Chemosphere* **2018**, *206*, 709–717. [CrossRef]

8.  Aziz, H.A.; Abu Amr, S.S. *Advanced Oxidation Processes (AOPs) in Water and Wastewater Treatment*; IGI Global: Hershey, PA, USA, 2019. [CrossRef]

9.  Trapido, M.; Tenno, T.; Goi, A.; Dulova, N.; Kattel, E.; Klauson, D.; Klein, K.; Tenno, T.; Viisimaa, M. Bio-recalcitrant pollutants removal from wastewater with combination of the Fenton treatment and biological oxidation. *J. Water Process Eng.* **2017**, *16*, 277–282. [CrossRef]

10. Amor, C.; Rodríguez-Chueca, J.; Fernandes, J.L.; Domínguez, J.R.; Lucas, M.S.; Peres, J.A. Winery wastewater treatment by sulphate radical based-advanced oxidation processes (SR-AOP): Thermally vs UV-assisted persulphate activation. *Process Saf. Environ. Prot.* **2019**, *122*, 94–101. [CrossRef]

11. Lucas, M.S.; Peres, J.A. Removal of Emerging Contaminants by Fenton and UV-Driven Advanced Oxidation Processes. *Water Air Soil Pollut.* **2015**, *226*, 273. [CrossRef]

12. Rodríguez-Chueca, J.; Amor, C.; Mota, J.; Lucas, M.S.; Peres, J.A. Oxidation of winery wastewater by sulphate radicals: Catalytic and solar photocatalytic activations. *Environ. Sci. Pollut. Res.* **2017**, *24*, 22414–22426. [CrossRef]

13. Lucas, M.S.; Peres, J.A.; Li Puma, G. Treatment of winery wastewater by ozone-based advanced oxidation processes ($O_3$, $O_3$/UV and $O_3$/UV/$H_2O_2$) in a pilot-scale bubble column reactor and process economics. *Sep. Purif. Technol.* **2010**, *72*, 235–241. [CrossRef]

14. Amor, C.; Lucas, M.S.; García, J.; Dominguez, J.R.; De Heredia, J.B.; Peres, J.A. Combined treatment of olive mill wastewater by Fenton's reagent and anaerobic biological process. *J. Environ. Sci. Health Part A* **2015**, *50*, 161–168. [CrossRef]

15. Rodríguez-Chueca, J.; Amor, C.; Fernandes, J.R.; Tavares, P.B.; Lucas, M.S.; Peres, J.A. Treatment of crystallized-fruit wastewater by UV-A LED photo-Fenton and coagulation–flocculation. *Chemosphere* **2016**, *145*, 351–359. [CrossRef]

16. Brink, A.; Sheridan, C.; Harding, K. Combined biological and advance oxidation processes for paper and pulp effluent treatment. *South Afr. J. Chem. Eng.* **2018**, *25*, 116–122. [CrossRef]

17. M'Arimi, M.M.; Mecha, C.A.; Kiprop, A.K.; Ramkat, R. Recent trends in applications of advanced oxidation processes (AOPs) in bioenergy production: Review. *Renew. Sustain. Energy Rev.* **2020**, *121*, 109669. [CrossRef]

18. Luo, H.; Zeng, Y.; He, D.; Pan, X. Application of iron-based materials in heterogeneous advanced oxidation processes for wastewater treatment: A review. *Chem. Eng. J.* **2020**. [CrossRef]

19. Rueda Márquez, J.J.; Levchuk, I.; Sillanpää, M. Application of Catalytic Wet Peroxide Oxidation for Industrial and Urban Wastewater Treatment: A Review. *Catalysts* **2018**, *8*, 673. [CrossRef]

20. Gil, A.; Galeano, L.A.; Vicente, M.Á. *Applications of Advanced Oxidation Processes (AOPs) in Drinking Water Treatment*; Springer International Publishing: New York, NY, USA, 2018. [CrossRef]

21. Ameta, S.C.; Ameta, R. *Advanced Oxidation Processes for Wastewater Treatment: Emerging Green Chemical Technology*; Elsevier Science: Amsterdam, The Netherlands, 2018; ISBN 9780128105252.

22. Santos Silva, A.; Seitovna Kalmakhanova, M.; Kabykenovna Massalimova, B.G.; Sgorlon, J.; Jose Luis, D.T.; Gomes, H.T. Wet Peroxide Oxidation of Paracetamol Using Acid Activated and Fe/Co-Pillared Clay Catalysts Prepared from Natural Clays. *Catalysts* **2019**, *9*, 705. [CrossRef]

23. Ormad, M.P.; Mosteo, R.; Ibarz, C.; Ovelleiro, J.L. Multivariate approach to the photo-Fenton process applied to the degradation of winery wastewaters. *Appl. Catal. B Environ.* **2006**, *66*, 58–63. [CrossRef]

24. Khare, P.; Patel, R.K.; Sharan, S.; Shankar, R. 8—Recent trends in advanced oxidation process for treatment of recalcitrant industrial effluents. In *Advanced Oxidation Processes for Effluent Treatment Plants*; Shah, M.P., Ed.; Elsevier: Amsterdam, The Netherlands, 2021; pp. 137–160. [CrossRef]

25. Jaén-Gil, A.; Buttiglieri, G.; Benito, A.; Mir-Tutusaus, J.A.; Gonzalez-Olmos, R.; Caminal, G.; Barceló, D.; Sarrà, M.; Rodriguez-Mozaz, S. Combining biological processes with UV/$H_2O_2$ for metoprolol and metoprolol acid removal in hospital wastewater. *Chem. Eng. J.* **2021**, *404*, 126482. [CrossRef]

26. Giannakis, S.; Jovic, M.; Gasilova, N.; Pastor Gelabert, M.; Schindelholz, S.; Furbringer, J.-M.; Girault, H.; Pulgarin, C. Iohexol degradation in wastewater and urine by UV-based Advanced Oxidation Processes (AOPs): Process modeling and by-products identification. *J. Environ. Manag.* **2017**, *195*, 174–185. [CrossRef]

27. Guimarães, V.; Teixeira, A.R.; Lucas, M.S.; Silva, A.M.T.; Peres, J.A. Pillared interlayered natural clays as heterogeneous photocatalysts for $H_2O_2$-assisted treatment of a winery wastewater. *Sep. Purif. Technol.* **2019**, *228*, 115768. [CrossRef]

28. Guimarães, V.; Lucas, M.S.; Peres, J.A. Combination of adsorption and heterogeneous photo-Fenton processes for the treatment of winery wastewater. *Environ. Sci. Pollut. Res.* **2019**, *26*, 31000–31013. [CrossRef]

29. Domínguez, C.M.; Quintanilla, A.; Casas, J.A.; Rodriguez, J.J. Treatment of real winery wastewater by wet oxidation at mild temperature. *Sep. Purif. Technol.* **2014**, *129*, 121–128. [CrossRef]

30. Mosteo, R.; Ormad, P.; Mozas, E.; Sarasa, J.; Ovelleiro, J.L. Factorial experimental design of winery wastewaters treatment by heterogeneous photo-Fenton process. *Water Res.* **2006**, *40*, 1561–1568. [CrossRef]

31. Tyagi, B.; Sidhpuria, K.; Shaik, B.; Jasra, R.V. Synthesis of Nanocrystalline Zirconia Using Sol–Gel and Precipitation Techniques. *Ind. Eng. Chem. Res.* **2006**, *45*, 8643–8650. [CrossRef]

32. Samadi, S.; Yousefi, M.; Khalilian, F.; Tabatabaee, A. Synthesis, characterization, and application of Nd, Zr–$TiO_2$/$SiO_2$ nanocomposite thin films as visible light active photocatalyst. *J. Nanostruct. Chem.* **2015**, *5*, 7–15. [CrossRef]

33. Sayagués, M.J.; Avilés, M.A.; Córdoba, J.M.; Gotor, F.J. Self-propagating combustion synthesis via an MSR process: An efficient and simple method to prepare (Ti, Zr, Hf)$B_2$–$Al_2O_3$ powder nanocomposites. *Powder Technol.* **2014**, *256*, 244–250. [CrossRef]

34. Teymourian, H.; Salimi, A.; Firoozi, S.; Korani, A.; Soltanian, S. One-pot hydrothermal synthesis of zirconium dioxide nanoparticles decorated reduced graphene oxide composite as high performance electrochemical sensing and biosensing platform. *Electrochim. Acta* **2014**, *143*, 196–206. [CrossRef]

35. Rajabi, M.; Khodai, M.M.; Askari, N. Microwave-assisted sintering of Al–$ZrO_2$ nano-composites. *J. Mater. Sci. Mater. Electron.* **2014**, *25*, 4577–4584. [CrossRef]

36. Sannino, D.; Vaiano, V.; Ciambelli, P.; Isupova, L.A. Mathematical modelling of the heterogeneous photo-Fenton oxidation of acetic acid on structured catalysts. *Chem. Eng. J.* **2013**, *224*, 53–58. [CrossRef]

37. He, J.; Yang, X.; Men, B.; Wang, D. Interfacial mechanisms of heterogeneous Fenton reactions catalyzed by iron-based materials: A review. *J. Environ. Sci.* **2016**, *39*, 97–109. [CrossRef]

38. Kalmakhanova, M.S.; Diaz de Tuesta, J.L.; Massalimova, B.K.; Gomes, H.T. Pillared clays from natural resources as catalysts for catalytic wet peroxide oxidation: Characterization and kinetic insights. *Environ. Eng. Res.* **2020**, *25*, 186–196. [CrossRef]

39. Rache, M.L.; García, A.R.; Zea, H.R.; Silva, A.M.T.; Madeira, L.M.; Ramírez, J.H. Azo-dye orange II degradation by the heterogeneous Fenton-like process using a zeolite Y-Fe catalyst—Kinetics with a model based on the Fermi's equation. *Appl. Catal. B Environ.* **2014**, *146*, 192–200. [CrossRef]

40. Ghime, D.; Ghosh, P. Decolorization of diazo dye trypan blue by electrochemical oxidation: Kinetics with a model based on the Fermi's equation. *J. Environ. Chem. Eng.* **2020**, *8*, 102792. [CrossRef]

41. Herney-Ramirez, J.; Silva, A.M.T.; Vicente, M.A.; Costa, C.A.; Madeira, L.M. Degradation of Acid Orange 7 using a saponite-based catalyst in wet hydrogen peroxide oxidation: Kinetic study with the Fermi's equation. *Appl. Catal. B Environ.* **2011**, *101*, 197–205. [CrossRef]

42. Silva, A.M.T.; Herney-Ramirez, J.; Söylemez, U.; Madeira, L.M. A lumped kinetic model based on the Fermi's equation applied to the catalytic wet hydrogen peroxide oxidation of Acid Orange 7. *Appl. Catal. B Environ.* **2012**, *121–122*, 10–19. [CrossRef]

43. Chapman, H.D. Cation exchange capacity. *Methods Soil Anal. Chem. Microbiol. Prop.* **1965**, *9*, 891–901.

44. APHA. *Standard Methods for the Examination of Water and Wastewater*, 21st ed.; American Public Health Association: Washington, DC, USA, 2005.

45. Lowry, O.H.; Rosebrough, N.J.; Farr, A.L.; Randall, R.J. Protein measurement with the Folin phenol reagent. *J. Biol. Chem* **1951**, *193*, 265–275.

46. Molina, C.B.; Casas, J.A.; Zazo, J.A.; Rodríguez, J.J. A comparison of Al-Fe and Zr-Fe pillared clays for catalytic wet peroxide oxidation. *Chem. Eng. J.* **2006**, *118*, 29–35. [CrossRef]

47. Guimarães, V.; Rodríguez-Castellón, E.; Algarra, M.; Rocha, F.; Bobos, I. Influence of pH, layer charge location and crystal thickness distribution on U(VI) sorption onto heterogeneous dioctahedral smectite. *J. Hazard. Mater.* **2016**, *317*, 246–258. [CrossRef]

48. Wang, Y.; Wang, W.; Wang, A. Efficient adsorption of methylene blue on an alginate-based nanocomposite hydrogel enhanced by organo-illite/smectite clay. *Chem. Eng. J.* **2013**, *228*, 132–139. [CrossRef]

49. Hou, B.; Han, H.; Jia, S.; Zhuang, H.; Xu, P.; Wang, D. Heterogeneous electro-Fenton oxidation of catechol catalyzed by nano-Fe$_3$O$_4$: Kinetics with the Fermi's equation. *J. Taiwan Inst. Chem. Eng.* **2015**, *56*, 138–147. [CrossRef]

50. Zhou, J.; Wu, P.; Dang, Z.; Zhu, N.; Li, P.; Wu, J.; Wang, X. Polymeric Fe/Zr pillared montmorillonite for the removal of Cr(VI) from aqueous solutions. *Chem. Eng. J.* **2010**, *162*, 1035–1044. [CrossRef]

51. Carriazo, J.G.; Guelou, E.; Barrault, J.; Tatibouët, J.M.; Moreno, S. Catalytic wet peroxide oxidation of phenol over Al–Cu or Al–Fe modified clays. *Appl. Clay Sci.* **2003**, *22*, 303–308. [CrossRef]